Spin wave modes in out-of-plane magnetized nanorings

X. Zhou,[1] E. V. Tartakovskaya,[2,3] G. N. Kakazei,[4] and A. O. Adeyeye[1]

[1]*Department of Electrical and Computer Engineering, National University of Singapore, 4 Engineering Drive 3, Singapore 117576, Singapore*

[2]*Institute of Magnetism, National Academy of Sciences of Ukraine, 36b Vernadskogo Blvd, 03142 Kiev, Ukraine*

[3]*Institute of High Technologies, Taras Shevchenko National University of Kiev, 03022 Kiev, Ukraine*

[4]*IFIMUP and IN-Institute of Nanoscience and Nanotechnology, Departamento de Física, Universidade do Porto, 4169-007 Porto, Portugal*

(Received 11 April 2017; revised manuscript received 27 June 2017; published 28 July 2017)

We investigated the spin wave modes in flat circular permalloy rings with a canted external bias field using ferromagnetic resonance spectroscopy. The external magnetic field H was large enough to saturate the samples. For $\theta = 0^\circ$ (perpendicular geometry), three distinct resonance peaks were observed experimentally. In the case of the cylindrical symmetry violation due to H inclination from normal to the ring plane (the angle θ of H inclination was varied in the $0^\circ-6^\circ$ range), the splitting of all initial peaks appeared. The distance between neighbor split peaks increased with the θ increment. Unexpectedly, the biggest splitting was observed for the mode with the smallest radial wave vector. This special feature of splitting behavior is determined by the topology of the ring shape. Developed analytical theory revealed that in perpendicular geometry, each observed peak is a combination of signals from the set of radially quantized spin wave excitation with almost the same radial wave vectors, radial profiles, and frequencies, but with different azimuthal dependencies. This degeneracy is a consequence of circular symmetry of the system and can be removed by H inclination from the normal. Our findings were further supported by micromagnetic simulations.

DOI: 10.1103/PhysRevB.96.024446

I. INTRODUCTION

Ferromagnetic rings have attracted considerable attention in the last few decades due to their unique magnetic ground states and their potential use in a range of applications such as magnetic random access memory (MRAM) [1–3], biomedical sensing [4,5], and magnetic logics [6]. By varying the inner and outer radii of the ring [7,8], its composition (number, thickness, and material of layers) [9,10], and by introducing structural defects [11,12], both static and dynamic magnetic properties in rings have been shown to be modified significantly. This high tunability leads to intensive investigations of microrings and nanorings [13], particularly the stability of magnetic configuration [14], magnetization reversal [15], and the nucleation and velocity of domain walls [16–18].

Investigations of dynamic behaviors of ring elements usually focus on spin wave (SW) spectra at remanence (vortex or onion states) [19–22] or in the tangential geometry, where the external field is applied in the ring plane [22]. The first experimental data of rings' magnetization dynamics in the close-to-perpendicular geometry that we presented recently [23] showed unusual SW spectra with multiple splitting. The configuration of the modes' splitting in rings is conceptually different from the splitting in nanostructures of the similar symmetry, i.e., in cylindrical nanowires [24] and circular nanodots [25].

Splitting of SW excitation spectra is a common effect in nanostructures both at remanence (for instance, vortex) and in the saturated state, though the background of this phenomenon can be different. For instance, in spectra of traveling modes of thin film, the splitting can appear due to patterning of films into antidot array [26] or due to the formation of periodic defects of different shapes [27]; the splitting of gyrotropic mode in ferromagnetic nanodisks with vortex ground state appears due to the difference between clockwise and counter-clockwise precession of vortex core [28–33]; for circular wires and dots in the saturated states, the splitting of SW modes occurs as a result of the external magnetic field canting from the axis of cylindrical symmetry [24,25]. There is a common rule for any case of localized SWs: Every degenerated mode of the symmetrical structure splits into a few modes if the symmetry is broken, and the number of split modes corresponds to the rank of degeneration of the initial mode. Therefore, to understand the origin of splitting spin excitations in nanorings due to the canted field, we should consider first the perfectly symmetrical case, i.e., SW spectra in perpendicular geometry.

In this paper, we give a comprehensive explanation of the SW spectra of the nanoring with the magnetic field applied out of plane. Values of SW frequencies received analytically, experimentally, and by computer simulations are in good agreement. Analytically calculated standing SW profiles are in quantitative agreement with corresponding simulation results. Specific feature of multiple splitting of SW spectra in rings with a canted magnetic field is explained on the basis of the analytical perturbation theory in the general context of the phenomenon of splitting in nanoparticles.

II. THEORETICAL BACKGROUND

The geometry of the ring structure and the corresponding coordinate system are presented in Fig. 1. We first consider the case of perpendicular geometry, in which the external field is parallel to the z axis (Fig. 1) and its value is high enough to keep the magnetization vector $\mathbf{M}$ perpendicular to the ring in the vast majority of the magnetic volume. In such a case, we can express magnetization as a sum of the saturation magnetization and a weakly excited component, $\mathbf{M} = M_0\mathbf{z} + \mathbf{m}$. In the SW approximation, the excitation term $\mathbf{m}$ has two spatial components, m_x and m_y.

To solve the problem of SW dynamics in the thin ring, we use the system of linearized Landau-Lifshitz (LL) equations

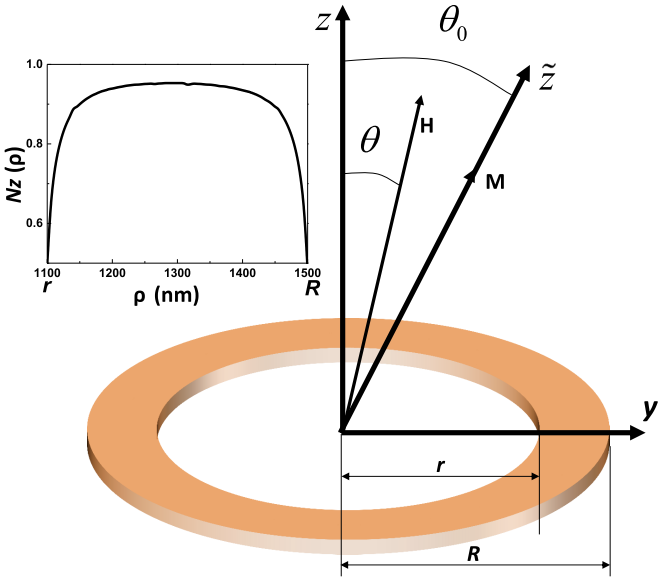

FIG. 1. Sketch of a thin circular nanoring and denominations of the angles in the canted geometry. Left inset: demagnetizing factor as a function of radial coordinate, where calculations were performed for the ring with inner radius $r = 1100$ nm, external radius $R = 1500$ nm, and thickness $a = 30$ nm.

with corresponding boundary conditions,

$$\frac{i\omega}{\gamma} m_x = \left(H_{\text{eff}} - \frac{2A}{M_0}\nabla^2 \right) m_y + M_0 \partial \Phi_M / \partial y$$

$$-\frac{i\omega}{\gamma} m_y = \left(H_{\text{eff}} - \frac{2A}{M_0}\nabla^2 \right) m_x + M_0 \partial \Phi_M / \partial x. \quad (1)$$

Here, the effective static field has a nonzero z component $H_{\text{eff}} = H + H_z$, which is the sum of the external field H and the spatially dependent z component of the static dipolar field $H_z = -M_0 \frac{\partial}{\partial z} \int_V d\mathbf{r}' \frac{\partial}{\partial z'} \frac{1}{|\mathbf{r}-\mathbf{r}'|}$, where the integration is performed over the volume (V) of the ring, M_0 is the saturation magnetization, A is the constant of inhomogeneous exchange interaction, presented in units erg cm^{-1}. The last terms in Eq. (1), which are proportional to $-\nabla\Phi_M$, describe the dynamic dipolar field generated by the magnetization precession with SW frequency ω. Φ_M is the dynamic part of the magnetic potential, which takes a form of the integral operator depending from the SW solution, $\Phi_M = \int_V d\mathbf{r}' (\mathbf{m} \cdot \nabla') \frac{1}{|\mathbf{r}-\mathbf{r}'|}$.

The exact analytical solution of LL integro-differential equation (1) for exchange-dipolar SW in nanostructures with strong inhomogeneities of dipolar fields is impossible in the majority of cases [34]. The unique event is the analytical solution for infinite cylindrical nanowires with magnetic field parallel to the wire's axis [35]. For confined three dimensional nonellipsoidal nanoparticles, such solutions are unknown. Even for systems with cylindrical symmetry, but violated translation symmetry, i.e., thin cylindrical nanodisks, the exact solution is impossible [36]. The approximate method, similar to the well-developed Ritz ansatz in quantum mechanics, is typically used in such a case. The main idea of this method is to find the trial solution, which should satisfy the boundary conditions and be in accordance with topology of the nanoparticle's shape. Then, the averaging of operator equation (1) with the corresponding basic functions should be done. In circular nanodisks, such approximate solutions are Bessel functions of the first kind, and corresponding standing SWs, by analogy with fundamental solutions of two-dimensional elastic membrane, were named "drum modes" [36]. A similar method was used in rectangular dots [37] and stripes [38], where plane waves are the basic functions for approximate solutions. Both complete orthonormal sets of functions (Bessel functions and plane waves) are the eigenfunctions of exchange operator and Zeeman term in Eq. (1) for corresponding cases in homogeneous external field. Summarizing, in very thin nanoparticles, where static dipolar field H_z is almost spatially constant, such basic functions are good approximate solutions of the LL equation (1) while taking into account the static demagnetizing field. However, eigenfunctions of the dipolar-dipolar integral operator are unknown in spatially confined nanoelements such as thin nanodisks, as well as in thin nanorings. Moreover, as our preliminary investigations have shown, the diagonalization of the dipolar-dipolar operator with Bessel functions as a basis is a rather slow convergent calculation procedure in the case of rings with the dimensions used in the present paper. This means that diagonal approximation, which can be considered as a natural consequence of the Ritz method [39–41], also cannot give the quantitatively reasonable results in such a case.

The way to avoid the mentioned difficulty was proposed in Ref. [36] for thin discs in perpendicular geometry. The main idea is based on the physically clear argument that the effect of dipolar-dipolar interaction in very thin planar nanoparticles should be numerically close to the same interaction in infinite thin film. In such a case, instead of the dynamic dipolar operator in LL Eq. (1), $-\nabla\Phi_M$, the matrix element of the dipole-dipole interaction for a perpendicularly magnetized film, $f(k) = 1 - \frac{(1-e^{-ka})}{ka}$, can be inserted. Here a is the thickness, and k is a radial component of the wave vector of the SW excitations of circular nanoparticles. Despite the inaccuracy of this approach, calculation of SW frequency gives a good fitting of experimental results. We will return to the calculations of SW frequency in Sec. V. Now we focus on the description of trial functions, corresponding SW profiles, and the discussion about the boundary conditions for SW excitations in thin nanorings.

Circular plane rings, which we consider in this paper, have the same cylindrical symmetry as circular dots and wires, so the Bessel functions are the first candidate to the role of trial functions in this case as well. However, it is worth noting that disks and rings are not of the topologically equivalent shapes. While the singularity at the disks' center excludes employing the Bessel functions of the second kind, the solution for SWs in magnetic rings can be written as a general solution of the Bessel equation, i.e., as a linear combination of Bessel functions of the first and the second kind. Such a solution is well-known in the theory of elastic membranes of ring shape.

Due to the small thickness of the ring, we can assume that the spin excitation profiles, as well as static and dynamic dipolar fields, are homogeneous along the z axis. Taking into account all of the above mentioned arguments, magnetic excitations' profiles in thin circular rings can be presented by

products of ρ-dependent and φ-dependent components,

$$\mu_{m,n}(\rho,\varphi) = [J_n(k_{m,n}\rho) + C_{m,n}Y_n(k_{m,n}\rho)]\exp(in\varphi), \quad (2)$$

where the ρ-dependent term is a linear combination of n-order Bessel functions of the first and the second kind; the values of radial wave vectors of standing modes, $k_{m,n}$, depend on the boundary conditions at the inner edge of the ring with the radius r and the external edge, which has the radius R.

The main origin of pinning at the edges of nanoparticles is strong local inhomogeneity of demagnetizing field [42,43]. Such inhomogeneities arise at the external edges of thin circular dots [36,42] and lead to the pinning boundary conditions. In thin rings, this question demands additional analysis. For this purpose, we define the spatial behavior of demagnetizing field and its peculiarities at the external edge of the thin ring (where $\rho = R$) and at the inner edge ($\rho = r$).

We consider the z component of the dipolar field in a perpendicularly magnetized thin ring as a function of the radial coordinate ρ,

$$H_z(\rho) = -M_0\frac{\partial}{\partial z}\int_V d\mathbf{r}'\frac{\partial}{\partial z'}\frac{1}{|\mathbf{r}-\mathbf{r}'|} = -4\pi M_0 N_z(\rho), \quad (3)$$

where the expression for the demagnetizing tensor $N_z(\rho)$ takes the form

$$N_z(\rho) = s\int_0^\infty dt\, J_0\left(t\frac{\rho}{a}\right)\left(J_1(st) - \frac{r}{R}J_1\left(\frac{r}{R}st\right)\right)\frac{(1-e^{-t})}{t}, \quad (4)$$

where $s = \frac{R}{a}$ is the aspect ratio and a is the thickness of the ring. The calculations for $N_z(\rho)$ by formula (4) with dimensions $R = 1500\,\text{nm}$, $r = 1100\,\text{nm}$, and $a = 30\,\text{nm}$ as a function of the radial coordinate are presented in the inset of Fig. 1. As it follows, the dependence $N_z(\rho)$ at the inner edge ($\rho = 1100\,\text{nm}$) and the external edge ($\rho = 1500\,\text{nm}$), are strongly inhomogeneous, quite similar to each other, and, additionally, almost equal to $N_z(\rho)$ at the edges of the thin disk with the same thickness and radius $R = 1500\,\text{nm}$. It gives the evidence of the same strong dipolar pinning at the inner and the external edges of the ring. So, the same pinning boundary conditions can be applied at both edges. It is important to mention also that $N_z(\rho)$ is flat and an almost constant function of ρ everywhere except the vicinity of the edges. In such a case, Bessel functions are good approximate solutions of the LL equation (1), excluding the dipolar-dipolar term. This proves the possibility to use the combinations of Bessel functions (2) as approximate solutions for spin excitations in perpendicular geometry for thin rings with large aspect ratio s.

Applying pinning boundary conditions at both external and inner edges of the ring leads to the set of equations

$$\psi_n(\beta) = J_n(\beta)Y_n\left(\beta\frac{r}{R}\right) - Y_n(\beta)J_n\left(\beta\frac{r}{R}\right) = 0. \quad (5)$$

Here, index n specifies the equation and the corresponding order of Bessel functions employed in it. Finding the roots $\beta_{m,n}$ [the pair of the indices (m, n) means the mth root of the nth equation] of Eq. (5), we determine the radial wave vectors $k_{m,n} = \frac{\beta_{m,n}}{R}$ and the corresponding coefficients in the expressions for elementary excitations (2), $C_{m,n} = -\frac{J_n(\beta_{m,n})}{Y_n(\beta_{m,n})}$.

To show the relative positions of $\beta_{m,n}$, we present the functions $\psi_n(\beta)$, calculated with a concrete parameter $\frac{r}{R} = \frac{11}{15}$, in Fig. 2(a). Every zero defines the radial wave vector of the corresponding standing SW. Very close zeros $\beta_{m,n}$ of $\psi_n(\beta)$ with different indices n but with the same number m [the numbered $m = 1, 2, 3\ldots$ ovals in Fig. 2(a)] determine almost equal values of the radial wave vectors $k_{m,n} = \frac{\beta_{m,n}}{R}$. Moreover, the calculations by formula (2) show that profiles of modes with the same m but different n have very similar ρ dependence [Figs. 2(b)–2(f)]; therefore, these profiles differ only due to the standard (exponential) dependence from φ. Also, analyzing the symmetry of the profiles' shapes, which are presented in Fig. 2, we can conclude that only the modes with odd m ($m = 1, 3, 5\ldots$) can be, in principle, detected.

The observed peculiarities of the solutions can be explained as a direct consequence of basic properties of Bessel functions [44]. We should note that large values $\beta > 10$, where the first roots of Eq. (5) appear [Fig. 2(a)], are important in this case. At large values of argument, the next relations between Bessel functions take place:

$$-J_0(\beta) \approx J_2(\beta) \approx -J_4(\beta) \approx J_6(\beta)\ldots \approx Y_1(\beta)$$
$$\approx -Y_3(\beta) \approx Y_5(\beta) \approx -Y_7(\beta)\ldots$$

and

$$-J_1(\beta) \approx J_3(\beta) \approx -J_5(\beta) \approx J_7(\beta)\ldots$$
$$\approx -Y_0(\beta) \approx Y_2(\beta) \approx -Y_4(\beta) \approx Y_6(\beta)\ldots$$

These approximate expressions, inserted in Eqs. (2) and (5), explain closeness of zeros $\beta_{m,n}$ with different indices n but with the same m, as well as the similarity of corresponding SW profiles. However, this consideration is valid only if the parameter $\frac{r}{R}$ (the relation between inner and outer radii) is not small. Our calculations show that such effect takes place only if $0.6 < \frac{r}{R} < 1$, i.e., when the radius of the hole is not small in comparing with the outer radius of the ring. The dimensions of the rings employed in this paper evidently satisfy this condition.

Equivalence of radial wave vectors and profiles leads, in turn, to the almost equal resonance fields of excitations with equal frequencies, the same m and different n. In the perpendicular geometry, only the modes with $n = 0$ can be actually detected, but every such spin excitation is connected with a dense set of associated modes with very close radial wave vectors, frequencies, and resonance fields. It is worth noting that this is not degeneration in a strict sense, as the resonance fields of such modes are not *exactly* equal. However, our estimations for rings with mentioned geometrical parameters and standard magnetic parameters of permalloy give the maximal distance between resonance fields of the first five neighboring modes [Fig. 2(a)] less than 10 Oe. So, in the perpendicular geometry, when circular symmetry is not violated, every experimentally detected mode is degenerated by quantum number n many times. Apart from this, modes with $n \neq 0$ are degenerated twice as usual in a cylindrically symmetrical case due to the sinusoidal and cosinusoidal dependencies of the mode profile (2) from the azimuthal angle φ.

In the case of thin rings, where z dependence of spin excitations' profile is negligible, $\mu_{m,n}(\rho,\varphi)$ (2) is an

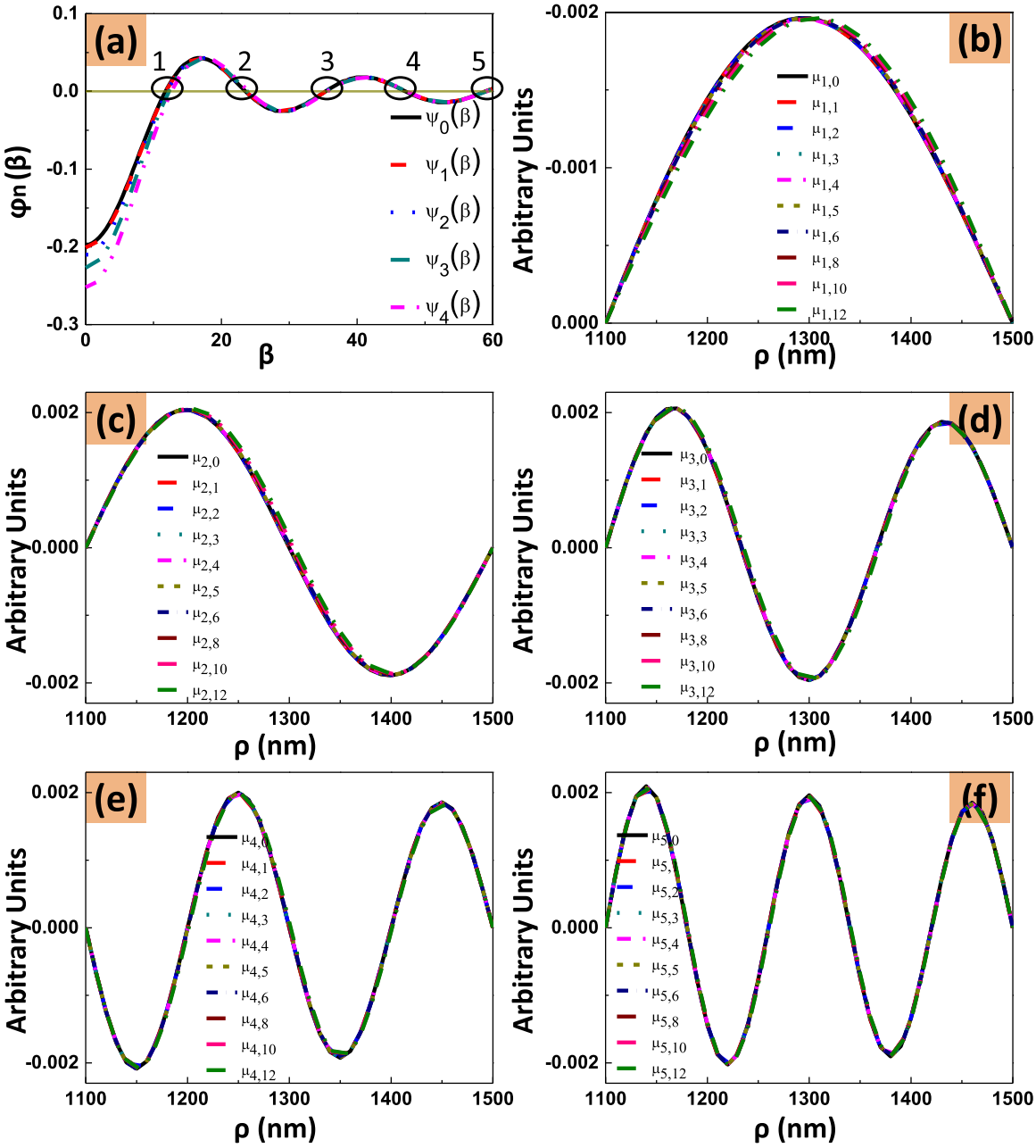

FIG. 2. Analytically calculated radial wave vectors and modes' profiles for perpendicularly magnetized nanorings. (a) Relative positions of zeros of the first five functions with different indices n [formula (5)], calculated for the value of the ratio $\frac{r}{R} = \frac{11}{15}$. Zeros of the same number m of different functions have very close values, as shown by black ovals. (b)–(f) Radial profiles of modes with $m = 1, 2, 3, 4$, and 5, calculated by formula (1) for a ring with the inner radius $r = 1100$ nm and the external radius $R = 1500$ nm.

eigenfunction of the two-dimensional Laplace operator, $\nabla^2\mu_{m,n}(\rho,\varphi) = -{k_{m,n}}^2\mu_{m,n}(\rho,\varphi)$. It should be noted that the value $k_{m,n}$, being a radial wave vector associating with the azimuthal number n, defines both the effects of the radial and the azimuthal dependencies of the profile on the exchange energy. Weak dependence of the $k_{m,n}$ from the number n is a natural consequence of the fact that in the chosen geometry of the nanoparticle, the SW energy is much more sensitive to the changes in the radial dependence of the SW profile than to the variations of its azimuthal part. However, for large values of n, the dependence of the SW energy from the azimuthal part of the profile becomes more considerable, and the distance between roots $\beta_{m,n}$ (with the same m but different n) enhances. In such a case, the split modes with the number (m, n) become hybridized with the modes with the number $m + 1$, and the term "degeneration" in perpendicular geometry loses the sense. But such effect takes place with the especially large values of n (in the case of the present parameters of the rings, our estimations show that $n > 16$) that corresponding modes have very small intensity. The situation is more complicated in the case when the external bias field is canted from the perpendicular direction. The modes with large n are undetectable due to their small intensity. However, as we show in the next sections of this article, the frequencies of SWs

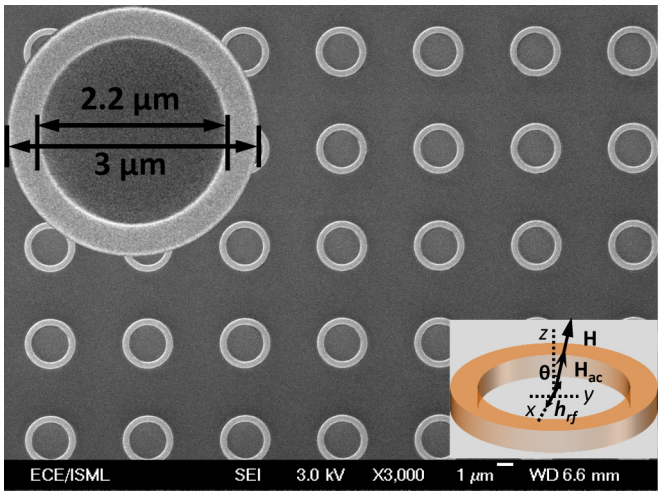

FIG. 3. The SEM image of the periodic array of permalloy rings. Top left inset: SEM image of the isolated ring with indicated dimensions. Bottom right inset: the geometry of the experiment.

depend on the angle of canting θ (Fig. 1). This leads to the considerable decreasing of the difference between frequencies of the modes with the numbers m and $m+1$ and the strong hybridization of corresponding split modes if the angle of canting $\theta > 4^\circ$.

If the symmetry is violated, for instance, by the canted external magnetic field, every single peak with one of the numbers $m = 1, 3, 5\ldots$ undergoes multiple splitting, like the mode with very high rank of degeneration. The radial dependencies of split modes' profiles with the same m are very close, while the dependencies from φ are different. Numerically, the mode with $m = 1$ should have the most considerable splitting, as the associated modes have larger difference of radial wave vectors [Fig. 2(a)] and of radial dependencies of profiles [Fig. 2(b)] than in the cases $m > 1$. However, the general behavior, i.e., the multiple splitting, is the same for all modes. Note, that the splitting under symmetry violation in circular submicron disks is quite different, i.e., there is a typical hierarchy: the first mode does not split, while the next modes split sequentially into odd numbers (3, 5, 7, etc.) of associated modes [25]. This difference of SW dynamics of rings and discs is originated from the difference of topology of discs' and rings' shapes, which gives the different expressions for boundary conditions for disks and rings even in the case of identical full pinning. In Sec. V, we will compare the results of analytical calculations employing the given approach with experimental data and computer simulations.

III. EXPERIMENTAL AND SIMULATION DETAILS

Large area ($4 \times 4\,\mathrm{mm}^2$) arrays of isolated permalloy circular rings were fabricated on a silicon substrate using deep ultraviolet (DUV) lithography at 248 nm exposure wavelength, followed by electron beam evaporation and ultrasonic assisted lift off process in OK73 resist thinner. Permalloy film with the thickness of 30 nm was deposited at a constant rate of 0.2 Å/s with a base pressure of 2×10^{-8} Torr. Details of the fabrication process are described elsewhere [45]. Shown as the top left inset in Fig. 3 is the representative scanning electron microscope (SEM) image of the 400-nm-wide circular ring with an outer diameter of 3 μm. The SEM images reveal good morphology and uniformity.

Perpendicular ferromagnetic resonance (pFMR) spectroscopy was used to characterize the dynamic response at room temperature. A 20 dBm microwave signal was generated by a continuous wave microwave generator at a specific frequency. The samples were placed on top of a 50 Ω microstrip line with the ring arrays facing the stripeline. The magnetic bias field (H) was swept from 18 kOe to 0 with an ac modulating field of ±20 Oe (H_{ac}) applied in the vicinity of the normal (defined as z direction). The inclination (defined as θ) of the external field with respect to z direction is varied from 0° to 6° with an angle step of 1°. A sketch of the field geometry is shown as the bottom right inset of Fig. 3. The output dc signal of the interferometric device is fed into a digital lock-in amplifier, which is locked to the field modulation signal. The FMR signal detected in this way represents the first derivative of the field sweeping absorption curve at a selected frequency.

To validate the experimental results, we also performed the dynamic micromagnetic simulation with the LLG micromagnetic simulator [46]. Standard parameters for permalloy (exchange constant $A = 1.30 \times 10^{-6}\,\mathrm{erg\,cm^{-1}}$, damping constant $\alpha = 0.01$, anisotropy constant $K_U = 0$, gyromagnetic ratio $\gamma = 2.9\,\mathrm{GHz\,kOe^{-1}}$, and saturation magnetization Ms = $745\,\mathrm{emu\,cm^{-3}}$, which is experimentally extracted by fitting the FMR results) were used for the simulation. The mask in the simulation was edge corrected and discretized by a unit cell size of 10 nm × 10 nm × 10 nm. For the quasistatic simulation, a damping coefficient of $\alpha = 1$ was chosen to obtain a rapid convergence. The FMR spectra were obtained by calculating the real part of the dynamic susceptibility. In our LLG simulation, the ac excitation field was set at 5 Oe. A larger ac field will introduce asymmetry of the profile of the simulated FMR spectra. To obtain the mode profiles, another dynamic simulation, where a flat top pulse with an amplitude of 20 Oe and pulse width of 50 ns was applied to the rings, was performed. The mode profiles were quantified by analyzing the results using spatially and frequency-resolved fast Fourier transform (FFT) imaging.

IV. EXPERIMENTAL RESULTS

Shown in Fig. 4 is the representative FMR absorption curve taken for 30-nm-thick rings at $f = 9$ GHz with the external magnetic field applied perpendicularly ($\theta = 0^\circ$) to the film plane. Similar to what has been reported before for dots and wires [36,47], a total number of up to three resonance modes are observed, with the first mode $H_{0-1} = 11.51$ kOe) exhibiting the highest intensity and the higher order modes ($H_{0-2} = 10.54$ kOe, $H_{0-3} = 9.82$ kOe) showing much smaller amplitudes. It is easy to understand that all the three modes are radially quantized standing SW modes with an increasing number of nodal lines.

However, when the external field is slightly canted, the profile of the absorption curve is significantly modified. Not only radially but azimuthally quantized SW modes are observed. Shown in Fig. 5 are the FMR absorption curves taken for $f = 9$ GHz with θ varied from 1° to 5° with an

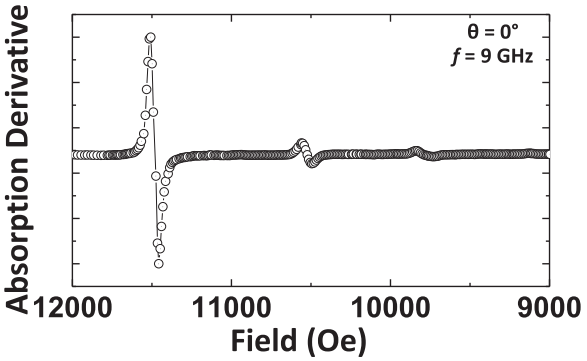

FIG. 4. The FMR absorption curve taken for the 30-nm-thick permalloy rings at $\theta = 0^\circ$ for $f = 9$ GHz.

increment of 2°. Different from the FMR curve observed at $\theta = 0^\circ$, the first two modes appearing at lower resonance fields ($H_{1-1} = 11.41$ kOe, $H_{1-2} = 10.49$ kOe) start to split for $\theta = 1^\circ$, and the splits become more obvious with the increase in the inclination. As the external field deviates further ($\theta = 3^\circ$), the resonance fields decrease drastically ($H_{3-1} = 11.11$ kOe, $H_{3-2} = 10.22$ kOe), while the number of splits increases. Shown as the insets are the zoom-in of the FMR absorption curves. For $\theta = 3^\circ$, we observed four splits for the first mode and more than five splits for the second mode. As the field is tilted by 5°, the resonance mode is shifted downwards by 520 Oe ($H_{5-1} = 10.59$ kOe) compared with $\theta = 3^\circ$. We also noticed that for $\theta = 5^\circ$, the number of splits for the first mode increased to five and the field gaps in between the splitting modes get larger. Taking the field difference in between the first two splits for the first mode for an example, the field gap increases from 124 Oe ($\theta = 3^\circ$) to 239 Oe ($\theta = 5^\circ$).

V. DISCUSSION AND CONCLUSION

Using the approximate solution (2) and applying the Ritz method to the LL equations (1) in perpendicular geometry, we

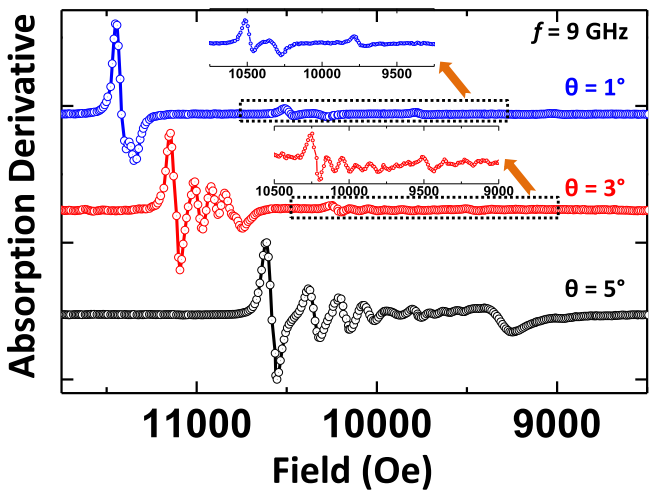

FIG. 5. The FMR absorption curves taken for the 30-nm-thick permalloy rings for $f = 9$ GHz with θ varied from 1° to 5°.

receive the Herring-Kittel SW dispersion relation [48],

$$\omega_{mn}^2 = \gamma^2\left[H_{nm} + \frac{2A}{M_0}{k_{mn}}^2\right] \times \left[H_{nm} + \frac{2A}{M_0}{k_{mn}}^2 + 4\pi M_0 \cdot f(k_{mn})\right], \quad (6)$$

with appropriately modified terms taking into account specific geometry of the magnetic ring. Here, $H_{nm} = H - 4\pi M_0 {N^z}_{mn}$ is the effective internal field, where the effective matrix element of the inhomogeneous demagnetizing field is

$${N^z}_{mn} = \frac{\int_r^R d\rho\rho|\mu_{m,n}(\rho,\varphi)|^2 N_z(\rho)}{4\pi \cdot \int_r^R d\rho\rho|\mu_{m,n}(\rho,\varphi)|^2}, \quad (7)$$

where $N_z(\rho)$ is the demagnetizing tensor of thin ring given by formula (4). The matrix element of dipole-dipole interaction for SWs has the standard form $f(k) = 1 - \frac{(1-e^{-ka})}{ka}$, as discussed in Sec. II. Due to the simple angular dependence $\mu_{m,n}(\rho,\varphi) \propto \exp(in\varphi)$ [see formula (2)], the integrand $|\mu_{m,n}(\rho,\varphi)|^2$ does not depend on φ for any n.

As already mentioned, index n can be replaced by 0 in the case of perpendicular geometry when only azimuthally symmetrical modes with $n = 0$ can be detected. However, as we have shown before [Fig. 2(a)], the radial wave vectors k_{mn} band together into groups that differ due to the index m. Inside every such group, k_{mn}, having the same m and different n, are almost equal. On the other hand, the ρ dependencies of the corresponding profiles $\mu_{m,n}(\rho,\varphi)$ are almost equal also [Figs. 2(b)–(f)]; this leads to equivalence of matrix elements N_{mn} with the same m and different n. As a result, the frequencies ω_{mn} described by expression (6) do not depend on the index n, corresponding to the strong degeneration of modes in perpendicular geometry, which we discussed in Sec. II.

Theoretically calculated resonance fields as a function of the excitation frequency by formulae (6)–(7) for three first azimuthally symmetrical modes $n = 0$, $m = 1, 3, 5$ are presented in Fig. 6 together with experimental data described

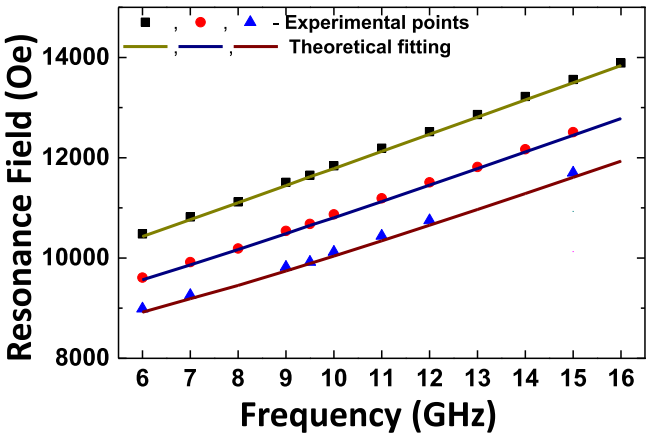

FIG. 6. Resonance fields extracted from spin wave excitations in thin ferromagnetic rings as a function of frequency for the three first modes ($m = 1, 3, 5$) in perpendicular geometry. Squares, round dots, and triangles: experimental data; solid lines: calculations by formulae (6)–(7) with radial wave vectors, numerically calculated roots of Eq. (5) [see Fig. 2(a)].

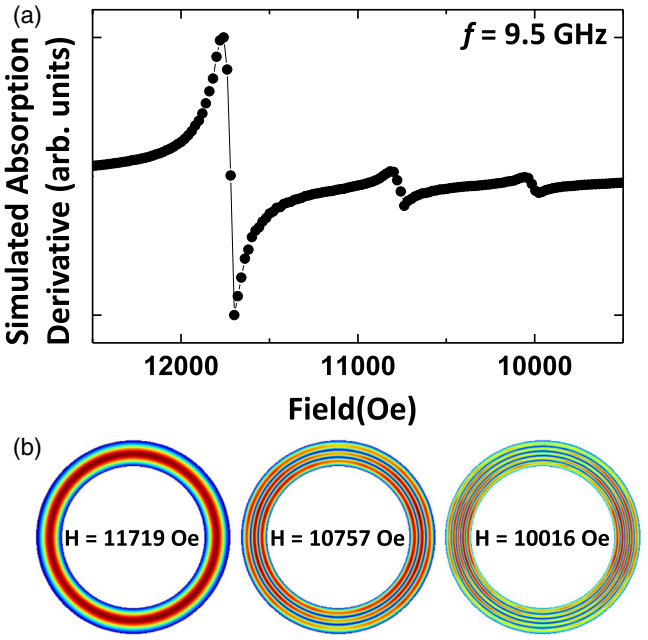

FIG. 7. (a) Simulation results of FMR absorption curve ($f = 9.5$ GHz, $\theta = 0^\circ$) and (b) excitations' profiles of three standing modes in perpendicularly magnetized nanoring.

in Sec. IV. As discussed above, these modes have the ρ-dependent profiles $\mu_{m,0}(\rho,\varphi) = J_0(k_{m,0}\rho) + C_{m,0}Y_0(k_{m,0}\rho)$, which are exhibited in Figs. 2(b), 2(d), and 2(f). Corresponding radial wave vectors are $k_{m,0} = \frac{\beta_{m,0}}{R}$, where $\beta_{m,0}$ are numerically calculated roots of Eq. (5) [they are within the ovals with numbers 1, 3, and 5 in Fig. 2(a)].

Good agreement between theoretical results and experimental data confirm the validity of the presented approach. Figure 7 shows the simulation results for 30-nm-thick permalloy rings at $f = 9.5$ GHz. Similar to the experimental results shown in Fig. 4, three resonance modes with nodal lines of $m = 1$, 3, and 5 are observed, and the intensity of these modes decreases with an increase in the number of nodal lines. Note that the ρ dependence of simulated profiles of three observed modes presented in Fig. 7(b) also agrees with analytically calculated profiles of observable modes, presented in Figs. 2(b), 2(d), and 2(f). Additionally, we make a detailed comparison of the experimental data, theoretical calculations, and results of computer simulations for $f = 9.5$ GHz. As shown in Table I, both the simulation and analytical results match quantitatively with the experimental values.

TABLE I. Resonance fields (all results are in Oe) at $f = 9.5$ GHz for three first modes: experimental data, computer simulation, and theoretical results are given together for comparison.

	$m = 1$	$m = 2$	$m = 3$
Experiment	11681	10700	9972
Simulation	11719	10757	10016
Theory	11615	10645	9890

We consider now the splitting of described modes due to the symmetry violation when the external field is canted from the perpendicular direction. The angle between $\boldsymbol{H}$ and the z direction, θ(Fig. 1), and the angle between $\boldsymbol{M}$ and the normal to the dot plane, θ_0, can be calculated from the balance between the Zeeman and magnetostatic energies, i.e., via minimizing the static magnetic energy

$$W(\theta,\theta_0) = -M_0 H\cos(\theta-\theta_0) + 2\pi M_0{}^2 N_z \cos(\theta_0)^2, \quad (8)$$

where the demagnetizing factor of the ring [49] is calculated by formula (9)

$$N_z = \frac{2}{1-(r/R)^2}\frac{R}{a}\int_0^\infty dq\,\frac{\left(J_1(q) - \frac{r}{R}J_1\left(\frac{r}{R}q\right)\right)^2}{q^2} \times (1-\exp(-qa/R)). \quad (9)$$

We present the analysis of SW excitations in such canted geometry only in the case of slight canting of the field and magnetization from the perpendicular direction, when the value of θ_0 can be considered as a small parameter. In the opposite case, i.e., when magnetization has a large tangential (parallel to the sample's plane) component, inhomogeneity of the demagnetizing field, $H_z(\rho)$, acts as an effective trap of the SW modes near particle's edges. This leads to the emergence of the edge modes in tangential geometry [50,51]. Such effect is beyond the scope of the present paper.

The SW excitation profiles of the same number m can be expressed as a superposition of interacting modes with different azimuthal φ dependence,

$$\mu_m(\rho,\varphi) = \sum_n (J_n(k_{m,n}\rho) + C_{m,n}Y_n(k_{m,n}\rho)) \times [A_n\cos(n\varphi) + B_n\sin(n\varphi)]. \quad (10)$$

The equivalence of radial wave vectors and profiles of such modes with equal m and different n (Sec. II, Fig. 2) leads to the simplification of the expression (10),

$$\mu_m(\rho,\varphi) \cong \bar{\mu}_m(\rho)\sum_n [A_n\cos(n\varphi) + B_n\sin(n\varphi)]. \quad (11)$$

We calculate resonance fields of modes with $m = 1$ and with the corresponding profile shown in Fig. 2(b) using the perturbation theory, which we developed in Ref. [25] for thin ferromagnetic dots, adapting it here for the particle of ring shape.

In the canted geometry (Fig. 1), the external field $\boldsymbol{H}$ and the magnetization $\boldsymbol{M}$ are confined in the zy plane. For further calculations, this is convenient to write LL in the "canted" system of coordinates, where the axis $\tilde{z}$ is directed along the canted vector $\boldsymbol{M}$, $m_{\tilde{y}}$ is a component of the variable magnetization along the $\tilde{y}$ axis of the canted coordinate system $(x\tilde{y}\tilde{z})$ (see Refs. [24] and [25])

$$\begin{aligned} &i\omega_k m_x - \gamma 4\pi M_0\cos(\theta_0) f_{xy}(m_x) \\ &= \gamma H^{\text{eff}}(\theta,\theta_0,\rho)m_{\tilde{y}} + \gamma 4\pi M_0[\sin^2(\theta_0) f_{zz}(m_{\tilde{y}}) \\ &\quad + \cos^2(\theta_0) f_{yy}(m_{\tilde{y}})] \\ &\quad - i\omega_k m_{\tilde{y}} - \gamma 4\pi M_0\cos(\theta_0) f_{xy}(m_{\tilde{y}}) \\ &= \gamma H^{\text{eff}}(\theta,\theta_0,\rho)m_x + \gamma 4\pi M_0 f_{xx}(m_x), \end{aligned} \quad (12)$$

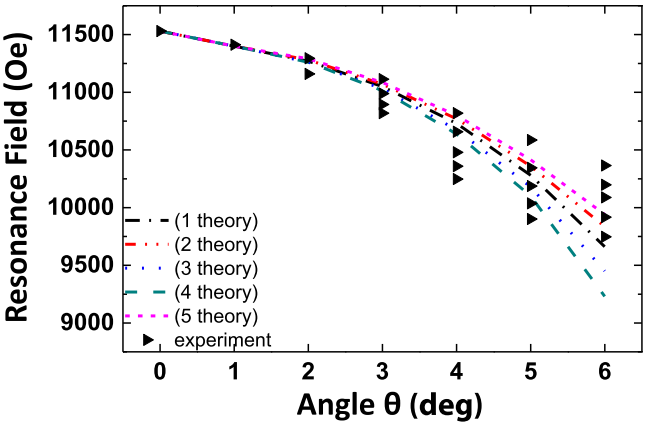

FIG. 8. Resonance fields of the modes ($f = 9$ GHz, $m = 1$) as a function of the angle θ. Lines: theoretical calculations for five modes with the lowest n ($n = 0,\ 2,\ 4$). Black triangles: experimental results.

In formula (12), the $\tilde{z}$ component of the effective field is

$$H^{\text{eff}}(\theta,\theta_0,\rho) = H\cos(\theta-\theta_0) + (H_z(\rho)\cos^2(\theta_0) - H_x(\rho)\sin^2(\theta_0)) + \frac{2A}{M_0}k^2, \tag{13}$$

where k is the radial wave vector of SW excitations and $H_i(\rho)$ is the component of the dipolar field. Specifics of calculations of $k = k_{mn}$ and $H_i(\rho)$ for rings' geometry were presented in Sec. II.

As verified for thin nanodots in perpendicular and slightly canted geometry (i.e., when the angle θ_0 is small), the dipolar operators can be substituted with c numbers in the framework of perturbation theory (Refs. [3] and [25]). We use the same approximation for thin rings, which leads to formulae $f_{zz} = 1 - f(k)$, $f_{yy} = f(k)\sin^2\varphi$, $f_{xx} = f(k)\cos^2\varphi$, $f_{xy} = f(k)\sin\varphi\cos\varphi$, where $f(k) = 1 - \frac{(1-e^{-ka})}{ka}$, φ is the azimuthal angle in the xy plane. This simplification allows us to receive such an equation for m_x,

$$\begin{aligned}\omega_k{}^2 m_x = {}& \gamma^2[H^{\text{eff}}(\theta,\theta_0,\rho) + 4\pi M_0\{\sin^2(\theta_0)(1-f(k)) \\ & + f(k)\}]H^{\text{eff}}(\theta,\theta_0,\rho)m_x + 4\pi\gamma^2 M_0\sin^2(\theta_0) \\ & \times(\{1-f(k)\}4\pi M_0 f(k)\cos^2(\varphi) - \sin^2(\varphi) \\ & \times f(k)H^{\text{eff}}(\theta,\theta_0,\rho))m_x\end{aligned} \tag{14}$$

In (14), the first term in the right part is axially symmetrical, while the second one is φ dependent. So, the second term describes differences of frequencies due to the dependence of modes' profiles from the azimuthal angle, as well as the interaction between modes with the same ρ dependence, but different φ dependence [see formula (11)]. As this stems from (11), any mode of concrete index m consists of an infinite number of associated modes with the same ρ dependence and different φ dependencies of profiles, which correspond to an infinite number of different indices n. At the same time, intensity of mode decreases when the index n increases. This simplifies the task, allowing us to restrict the infinite summation in (11) by few terms with the smallest n. Due to the dipolar interaction between these SW modes, which reveals itself when $\theta_0 \neq 0$ [see formula (15)], the degenerated level splits into the set of levels, and the value of this splitting increases with an enhancing of the angle θ.

Inserting basic states (11) into Eq. (14), we obtain an infinite system of linear equations for coefficients A_n and B_n. We then look for the approximate solution of the eigenvalue problem, using a finite subset of the basis states. Using the perturbation theory by θ_0, we calculate the frequencies of first five split modes by analytical diagonalization of corresponding five-rank matrix. The result is given by formulae (15),

$$\begin{aligned}
\omega_k{}^2 &= \omega_S{}^2 + \gamma^2 2\pi M_0\sin^2(\theta_0)\cdot f(k_{mn})\left(\{1-f(k_{mn})\}4\pi M_0 - H^{\text{eff}}_{mn}(\theta,\theta_0)\right) \\
\omega_k{}^2 &= \omega_S{}^2 + \gamma^2 2\pi M_0\sin^2(\theta_0)\cdot f(k_{mn})\left(\tfrac{1}{2}\{1-f(k_{mn})\}4\pi M_0 - \tfrac{3}{2}H^{\text{eff}}_{mn}(\theta,\theta_0)\right) \\
\omega_k{}^2 &= \omega_S{}^2 + \gamma^2 2\pi M_0\sin^2(\theta_0)\cdot f(k_{mn})\left(\tfrac{3}{2}\{1-f(k_{mn})\}4\pi M_0 - \tfrac{1}{2}H^{\text{eff}}_{mn}(\theta,\theta_0)\right) \\
\omega_k{}^2 &= \omega_S{}^2 + \gamma^2 2\pi M_0\sin^2(\theta_0)\cdot f(k_{mn})\left(\left(1+\tfrac{\sqrt{3}}{2}\right)\{1-f(k_{mn})\}4\pi M_0 - \left(1-\tfrac{\sqrt{3}}{2}\right)H^{\text{eff}}_{mn}(\theta,\theta_0)\right) \\
\omega_k{}^2 &= \omega_S{}^2 + \gamma^2 2\pi M_0\sin^2(\theta_0)\cdot f(k_{mn})\left(\left(1-\tfrac{\sqrt{3}}{2}\right)\{1-f(k_{mn})\}4\pi M_0 - \left(1+\tfrac{\sqrt{3}}{2}\right)H^{\text{eff}}_{mn}(\theta,\theta_0)\right)
\end{aligned} \tag{15}$$

Here, $H^{\text{eff}}_{mn}(\theta,\theta_0) = (H_{mn}(\theta,\theta_0) + \frac{2A}{M_0}k_{mn}{}^2)$,

$$\omega_S{}^2 = \gamma^2\left[H^{\text{eff}}_{mn}(\theta,\theta_0) + 4\pi M_0\left\{\sin^2(\theta_0)(1-f(k_{mn})) + f(k_{mn})\right\}\right]\cdot H^{\text{eff}}_{mn}(\theta,\theta_0).$$

The matrix element of the effective internal field in the canted geometry takes the form (see Refs. [24], [25], and [52]): $H_{mn} \to H_{mn}(\theta,\theta_0) = H\cos(\theta-\theta_0) - 4\pi M_0(N^z{}_{mn}\cos^2(\theta_0) - N^x{}_{mn}\sin^2(\theta_0))$.

Results for excitations with $f = 9$ GHz are shown in Fig. 8. The difference between theoretical results and experimental data can be explained by the change of boundary conditions in the canted geometry [53], which we did not take into account.

Figure 9 shows the simulated FMR curve and the corresponding mode profiles for rings with the external field tilted by 5°. In agreement with the experimental observation, in the canted geometry, the first mode splits into five resonance modes. The extracted mode profiles [Fig. 9(b)] show that the splitting modes share the same radial profile but different azimuthal profiles. We also note that the modes with more azimuthal nodes, appearing at lower resonance fields, exhibit smaller mode intensities.

In conclusion, the canting of the external bias field leads to the splitting of the rings' SW modes. The general picture of the modes' splitting in rings is conceptually different from the splitting in cylindrical nanowires and circular nanodots. Namely, in rings every mode observed in perpendicular

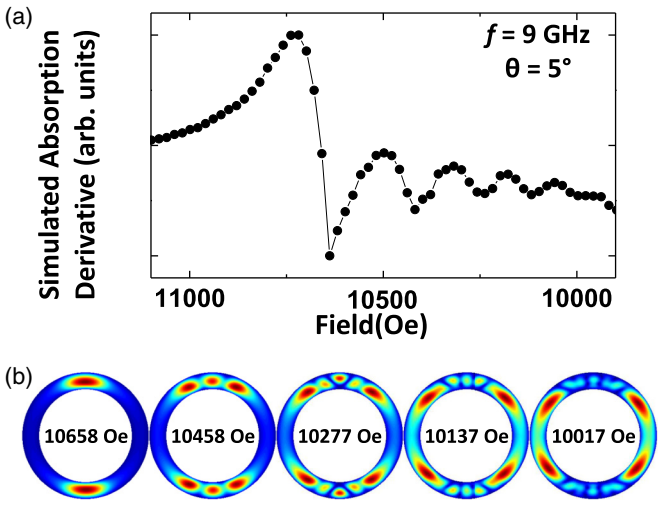

FIG. 9. (a) Simulation results of FMR absorption curve ($f = 9$ GHz, $\theta = 5^\circ$) and (b) excitations' profiles of azimuthally quantized standing modes.

geometry (including the first one) is splitting into large number of modes, which have the same radial profile but different azimuthal profiles. Since the intensity of split modes decreases with increase of azimuthal index, only several of the lowest modes can be observed in experiment and simulations. As the canting of the field gets larger, the distance between neighbor split peaks is increasing. Our analytical calculations and simulation results agree well with the experimental results.

ACKNOWLEDGMENTS

This paper was supported by the National Research Foundation, Prime Minister's Office, Singapore, under its Competitive Research Programme (CRP Award No. NRF-CRP 10-2012-03), the European Union's Horizon 2020 research and innovation program under Marie Skłodowska-Curie Grant No. 644348. G.N.K. acknowledges support from the Portuguese Foundation of Science and Technology (FCT) through Project No. EXPL/IF/00981/2013 and the "Investigador FCT" program. We are thankful to V. Tiberkevich, B. A. Ivanov, and V. O. Golub for fruitful discussions.

[1] F. J. Castano, C. A. Ross, C. Frandsen, A. Eilez, D. Gil, H. I. Smith, M. Redjdal, and F. B. Humphrey, Phys. Rev. B **67**, 184425 (2003).
[2] T. J. Hayward, J. Llandro, R. B. Balsod, J. A. C. Bland, D. Morecroft, F. J. Castaño, and C. A. Ross, Phys. Rev. B **74**, 134405 (2006).
[3] X. Zhu and J.-G. Zhu, IEEE Trans. Mag. **39**, 2854 (2003).
[4] M. M. Miller, G. A. Prinz, S.-F. Cheng, and S. Bounnak, Appl. Phys. Lett. **81**, 2211 (2002).
[5] J. Llandro, T. J. Hayward, D. Morecroft, J. A. C. Bland, F. J. Castaño, I. A. Colin, and C. A. Ross, Appl. Phys. Lett. **91**, 203904 (2007).
[6] S. R. Bowden and U. J. Gibson, J. Phys. Conf. Ser. **200**, 072033 (2010).
[7] H. Schultheiss, S. Schäfer, P. Candeloro, B. Leven, B. Hillebrands, and A. N. Slavin, Phys. Rev. Lett. **100**, 047204 (2008).
[8] L. Yong, D. Yan, and M. Veena, Nanotechnology **19**, 265301 (2008).
[9] C. A. Ross, F. J. Castano, W. Jung, B. G. Ng, I. A. Colin, and D. Morecroft, J. Phys. D: Appl. Phys. **41**, 113002 (2008).
[10] M. Madami, S. Tacchi, G. Gubbiotti, G. Carlotti, H. Pandana, R. D. Gomez, H. Tanigawa, and T. Ono, J. Appl. Phys. **104**, 063510 (2008).
[11] M. Kläui, C. A. F. Vaz, J. A. C. Bland, W. Wernsdorfer, G. Faini, and E. Cambril, J. Appl. Phys. **93**, 7885 (2003).
[12] F. Giesen, J. Podbielski, B. Botters, and D. Grundler, Phys. Rev. B **75**, 184428 (2007).
[13] X. L. Liu, Y. Yang, C. T. Ng, L. Y. Zhao, Y. Zhang, B. H. Bay, H. M. Fan, and J. Ding, Adv. Mater. **27**, 1939 (2015).
[14] S. Mamica, J. Appl. Phys. **113**, 093901 (2013).
[15] W. Zhang and S. Haas, Phys. Rev. B **81**, 064433 (2010).
[16] K. Richter, A. Krone, M.-A. Mawass, B. Krüger, M. Weigand, H. Stoll, G. Schütz, and M. Kläui, Phys. Rev. B **94**, 024435 (2016).
[17] K. Richter, A. Krone, M.-A. Mawass, B. Krüger, M. Weigand, H. Stoll, G. Schütz, and M. Kläui, Phys. Rev. Appl. **5**, 024007 (2016).
[18] A. L. Gonzalez Oyarce, T. Trypiniotis, P. E. Roy, and C. H. W. Barnes, Phys. Rev. B **87**, 174408 (2013).
[19] I. Neudecker, M. Kläui, K. Perzlmaier, D. Backes, L. J. Heyderman, C. A. F. Vaz, J. A. C. Bland, U. Rüdiger, and C. H. Back, Phys. Rev. Lett. **96**, 057207 (2006).
[20] G. Shimon, A. O. Adeyeye, and C. A. Ross, Phys. Rev. B **89**, 024302 (2014).
[21] J. Podbielski, F. Giesen, and D. Grundler, Phys. Rev. Lett. **96**, 167207 (2006).
[22] G. Gubbiotti, M. Madami, S. Tacchi, G. Carlotti, H. Tanigawa, T. Ono, L. Giovannini, F. Montoncello, and F. Nizzoli, Phys. Rev. Lett. **97**, 247203 (2006).
[23] X. Zhou, J. Ding, M. Kostylev, and A. O. Adeyeye, Appl. Phys. Lett. **106**, 112403 (2015).
[24] E. V. Tartakovskaya, Phys. Rev. B **71**, 180404 (2005).
[25] S. A. Bunyaev, V. O. Golub, O. Yu. Salyuk, E. V. Tartakovskaya, N. M. Santos, A. A. Timopheev, N. A. Sobolev, A. A. Serga, A. V. Chumak, B. Hillebrands, and G. N. Kakazei, Sci. Rep. **5**, 18480 (2015).
[26] R. A. Gallardo, A. Banholzer, K. Wagner, M. Körner, K. Lenz, M. Farle, J. Lindner, J. Fassbender, and P. Landeros, New J. Phys. **16**, 023015 (2014).
[27] S. McPhail, C. M. Gürtler, J. M. Shilton, N. J. Curson, and J. A. C. Bland, Phys. Rev. B **72**, 094414 (2005).
[28] F. Hoffmann, G. Woltersdorf, K. Perzlmaier, A. N. Slavin, V. S. Tiberkevich, A. Bischof, D. Weiss, and C. H. Back, Phys. Rev. B **76**, 014416 (2007).
[29] R. V. Verba, A. Hierro-Rodriguez, D. Navas, J. Ding, X. M. Liu, A. O. Adeyeye, K. Y. Guslienko, and G. N. Kakazei, Phys. Rev. B **93**, 214437 (2016).
[30] J. P. Park and P. A. Crowell, Phys. Rev. Lett. **95**, 167201 (2005).
[31] K. Y. Guslienko, A. N. Slavin, V. Tiberkevich, and S.-K. Kim, Phys. Rev. Lett. **101**, 247203 (2008).

[32] K. Y. Guslienko, G. R. Aranda, and J. M. Gonzalez, Phys. Rev. B **81**, 014414 (2010).
[33] A. A. Awad, K. Y. Guslienko, J. F. Sierra, G. N. Kakazei, V. Metlushko, and F. G. Aliev, Appl. Phys. Lett. **96**, 012503 (2010).
[34] M. Pardavi-Horvath and E. Tartakovskaya, in *Magnetic Nano- and Microwires. Design, Synthesis, Properties and Applications*, edited by M. Vázquez, Woodhead Publishing Series in Electronic and Optical Materials (Woodhead Publishing, Amsterdam, 2015), Chap. 23.
[35] R. Arias and D. L. Mills, Phys. Rev. B **63**, 134439 (2001).
[36] G. N. Kakazei, P. E. Wigen, K. Y. Guslienko, V. Novosad, A. N. Slavin, V. O. Golub, N. A. Lesnik, and Y. Otani, Appl. Phys. Lett. **85**, 443 (2004).
[37] C. Bayer, J. Jorzick, B. Hillebrands, S. O. Demokritov, R. Kouba, R. Bozinoski, A. N. Slavin, K. Y. Guslienko, D. V. Berkov, N. L. Gorn, and M. P. Kostylev, Phys. Rev. B **72**, 064427 (2005).
[38] K. L. Livesey, J. Ding, N. R. Anderson, R. E. Camley, A. O. Adeyeye, M. P. Kostylev, and S. Samarin, Phys. Rev. B **87**, 064424 (2013).
[39] K. Y. Guslienko and A. N. Slavin, J. Appl. Phys. **87**, 6337 (2000).
[40] B. A. Kalinikos and A. N. Slavin, J. Phys. C: Solid State Phys. **19**, 7013 (1986).
[41] E. V. Tartakovskaya, M. Pardavi-Horvath, and R. D. McMichael, Phys. Rev. B **93**, 214436 (2016).
[42] K. Y. Guslienko and A. N. Slavin, Phys. Rev. B **72**, 014463 (2005).
[43] B. A. Ivanov and C. E. Zaspel, Appl. Phys. Lett. **81**, 1261 (2002).
[44] N. N. Lebedev, *Special Functions and Their Applications* ([s.n.], Englewood Cliffs, 1965).
[45] A. O. Adeyeye and N. Singh, J. Phys. D: Appl. Phys. **41**, 153001 (2008).
[46] M. R. Scheinfein, LLG Micromagnetics Simulator, software for micromagnetic simulations, http://llgmicro.home.mindspring.com (date of access: 04.04.2014).
[47] X. Zhou and A. O. Adeyeye, Phys. Rev. B **94**, 054410 (2016).
[48] C. Herring and C. Kittel, Phys. Rev. **81**, 869 (1951).
[49] B. Leighton, O. J. Suarez, P. Landeros, and J. Escrig, Nanotechnology **20**, 385703 (2009).
[50] F. Guo, L. M. Belova, and R. D. McMichael, Phys. Rev. Lett. **110**, 017601 (2013).
[51] J. Jorzick, S. O. Demokritov, B. Hillebrands, M. Bailleul, C. Fermon, K. Y. Guslienko, A. N. Slavin, D. V. Berkov, and N. L. Gorn, Phys. Rev. Lett. **88**, 047204 (2002).
[52] O. Klein, G. deLoubens, V. V. Naletov, F. Boust, T. Guillet, H. Hurdequint, A. Leksikov, A. N. Slavin, V. S. Tiberkevich, and N. Vukadinovic, Phys. Rev. B **78**, 144410 (2008).
[53] G. N. Kakazei, G. R. Aranda, S. A. Bunyaev, V. O. Golub, E. V. Tartakovskaya, A. V. Chumak, A. A. Serga, B. Hillebrands, and K. Y. Guslienko, Phys. Rev. B **86**, 054419 (2012).